Counter-rotating eddy pair in the Luzon Strait

Sun Ruili[1,2*], Li Peiliang[1,3], GuYanzhen[3], Zhai Fangguo[4], Yan Yunwei[2], Li Bo[5]

[1]Hainan Institute of Zhejiang University, Sanya, Hainan, China

[2]State Key Laboratory of Satellite Ocean Environment Dynamics, Second Institute of

Oceanography, Ministry of Natural Resources, Hangzhou, China

[3]Ocean college, Zhejiang University, Zhoushan, China

[4]College of Oceanic and Atmospheric Sciences, Ocean University of China, Qingdao, China

[5]State Key Laboratory of Tropical Oceanography, South China Sea Institute of Oceanology,

Chinese Academy of Sciences, Guangzhou, China

Corresponding author:Sun Ruili, sunruili2007@126.com

Abstract:

Based on satellite remote-sensing observation data and Hybrid Coordinate Ocean Model (HYCOM) re-analysis data, we studied the counter-rotating eddy pair in the Luzon Strait (LS). Statistical analysis reveals that when an anti-cyclonic mesoscale eddy (AE) (cyclonic mesoscale eddy [CE]) in the Northwest Pacific (NWP) gradually approaches the east side of the LS, a CE (an AE) gradually forms on the west side of the LS, and it is defined as the AE (CE) mode of the counter-rotating eddy pair in the LS. The counter-rotating eddy pair exhibits obvious seasonal variation: the AE mode mainly occurs in the summer half of the year, while the CE mode mainly occurs in the winter half of the year. The mean durations of the AE and CE modes are both approximately 70 d. Based on vorticity budget equation and energy analysis, the dynamic mechanism of counter-rotating eddy-pair occurrence is determined to be as follows: the AE (CE)

23 on the east side of the LS causes a positive (negative) vorticity anomaly through horizontal

24 velocity shear on the west side of the LS, and the positive (negative) vorticity anomaly is

25 transported westward by the zonal advection of the vorticity, finally leading to the formation of the

26 CE (AE) on the west side of the LS.

27 **Keywords:** counter-rotating eddy pair; Luzon Strait; vorticity budget equation; barotropic

28 instability

29 **1 Introduction**

30   The Luzon Strait (LS), located between the island of Taiwan and Luzon Island, is an important

31 gap for particle and energy exchange between the South China Sea (SCS) and Northwest Pacific

32 (NWP). The topography around the LS is very complicated. The LS is composed of three straits

33 from north to south: Bashi Strait, Balintang Strait, and Babuyan Strait. The Batanes Islands and

34 Babuyan Islands are located in these straits (Figure 1). This complex topography leads to the

35 generation and aggregation of a large number of mesoscale eddies, which then play an important

36 role in the dynamic ocean process around the LS (Liu *et al.*, 2012; Lu and Liu, 2013; Sun *et al.*,

37 2016a; Sun *et al.*, 2020).

38   Mesoscale eddies interaction is an important focus of previous studies on mesoscale eddies in

39 the LS. Jing and Li (2003) used satellite remote-sensing observation data to discover a cyclonic

40 mesoscale cold eddy around Lanyu Island to the northeast of the LS. They pointed out that the

41 formation of the Lanyu cold eddy was the result of the joint action of the meandering Kuroshio

42 overshooting and conservation of the potential vorticity. Sun *et al.* (2016b) believed that the

43 formation of the Lanyu cold eddy was a process of eddies-eddies interaction. They used satellite

44 observation data and composition analysis to study the Lanyu cold-eddy phenomenon, and pointed

45 out that the combined action of the Kuroshio loop (cyclonic circulation) and an AE from the NWP

46 led to the formation of the Lanyu cold eddy. Based on satellite observation data, *in situ*

47 observation data and numerical modelling data, Zhang *et al.* (2017) studied mesoscale

48 eddies-eddies interaction to the northwest of the LS. They analyzed the energy budget of the

49 Kuroshio invading the SCS, and determined that the northern branch of the anti-cyclonic

50 circulation caused by the Kuroshio loop had a large horizontal shear stress and thus led to the

51 formation of a CE southwest of Taiwan Island through the barotropic instability.

52   Previous studies showed that mesoscale eddies-eddies interaction can cause particle and

53 energy exchange and often occurs in the vicinity of the LS (Sun *et al*., 2016b; Zhang *et al*., 2017;

54 Sun *et al*., 2018). Since the LS is an important gap for particle and energy exchange between the

55 SCS and NWP, a logical question is whether this phenomenon of mesoscale eddies-eddies

56 interaction can occur on the east and west sides of the LS and whether it plays an important role in

57 the particle and energy exchange between the SCS and NWP. To explore this issue, we compare

58 sea-surface height anomaly (SSHA) distributions in the SCS when a CE occurs and when an AE

59 occurs on the east side of the LS (Figure 2). The specific process is described in detail in Section

60 3.1. Figure 2 shows that when an AE (a CE) occurs on the east side of the LS, a CE (an AE) forms

61 on the west side of the LS, which was observed in the in-situ observation data (Huang *et al*., 2019).

62 This is referred to in this article as the counter-rotating eddy-pair phenomenon.

63   To our knowledge, this is the first time a counter-rotating eddy-pair phenomenon in the LS

64 has been proposed, which creates a new form of particle and energy exchange between the SCS

65 and the NWP. The present study will supplement and perfect the theory of particle and energy

66 exchange between the SCS and NWP. We give the statistical characteristics and dynamic

67 mechanism of this phenomenon herein. The rest of this paper is organized as follows. Section 2

68 briefly introduces the data and methods, Section 3 presents the research results, and Section 4

69 provides a discussion and conclusion.
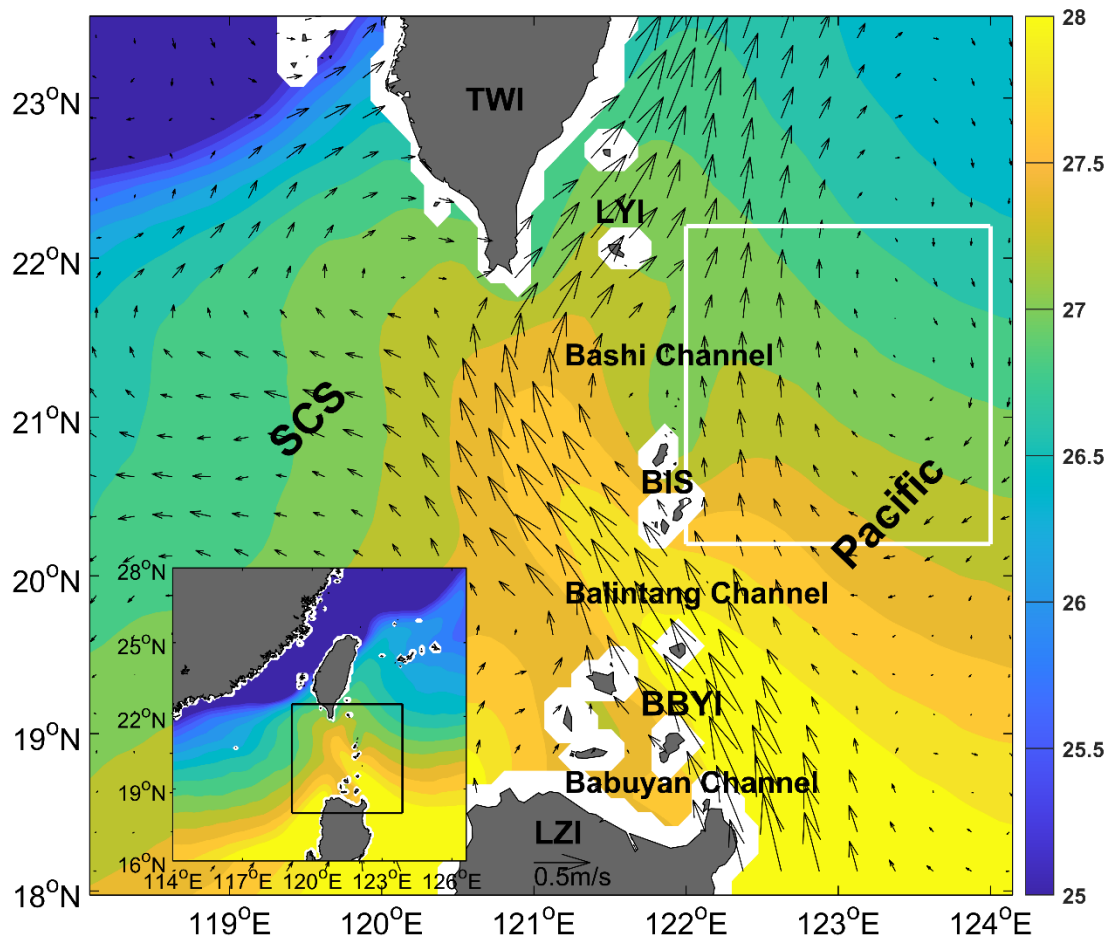
71 Figure 1. Climate state of spatial distribution of RSS SST (°C; shading) and CMEMS geostrophic

72 current (m/s; vectors) from 2003 to 2020. SCS, South China Sea; BIS, Batanes Islands; TWI,

73 Taiwan Island; LZI, Luzon Island; BBYI, Babuyan Islands; LYI, Lanyu Island. White box borders

74 20.2–22.2°N, 122–124°E. Extent of the main map is shown as black-bordered box in inset.

75
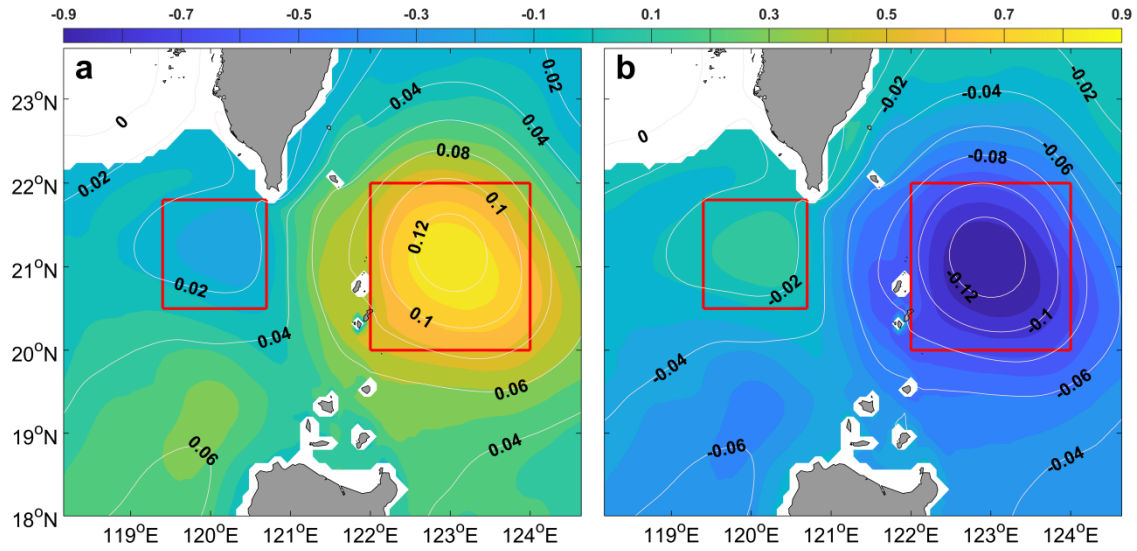
76

77 Figure 2. Spatial distribution of counter-rotating eddy pair in the LS. Spatial patterns of AE (a) and

78 CE (b) modes. Panel a (b) corresponds to average state when an AE (a CE) occurred in area

79 marked by red box on east side of LS from 1993 to 2020. Contours represent SSHA (units of m).

80 Colors represent sea temperature anomaly (units of °C) at a depth of 300 m. Interval of SSHA is

81 0.03 m. Red boxes on west and east sides of LS border mark 20.5–21.8°N, 119.4–120.7°E and 20–

82 22°N, and 122–124°E, respectively. Figure is similar to Figure 3 of Sun *et al*. (2018), and is based

83 on HYCOM data.

84 **2 Data and methods**

85 2.1 Data

86 Satellite remote-sensing SSHA, geostrophic current, and geostrophic current anomaly data

87 were provided by the Copernicus Marine Environment Monitoring Service (CMEMS). The dataset

88 was generated by the processing system including data from all altimeter missions: Sentinel-3A/B,

89 Jason-3, HY-2A, Cryosat-2, OSTM/Jason-2, Jason-1, Topex/Poseidon, Envisat, GFO, and

90 ERS-1/2. The dataset provides global coverage data from January 1, 1993 to August 2, 2021, with

91 a spatial resolution of 0.25°×0.25° and temporal sampling frequency of 1 d. It also provides one

92   near-real-time component and one delayed-time component. The delayed-time component has

93   been inter-calibrated and provides a homogeneous and highly accurate, long time series of all

94   altimeter data (Pujol and Francoise, 2019), and is chosen for use in this paper.

95   Model data are obtained from the Hybrid Coordinate Ocean Model (HYCOM) model output

96   by the U.S. Naval Research Laboratory. The dataset is based on ocean prediction system output,

97   and the product with the longest time span from 2 October 1992 to 31 December 2012 was chosen

98   from all HYCOM data-assimilation products provided by the HYCOM organization. The dataset

99   is based on ocean prediction system output with a spatial resolution of $0.08°×0.08°$ and 40

100   standard z levels between 80.48°S and 80.48°N. It provides temperature, salinity, sea-surface

101   height, zonal flow, and meridional flow (Wallcraft *et al*., 2003).

102   The wind dataset was provided by the National Centers for Environmental Information

103   (NCEI). The dataset merges multiple satellite observations with *in situ* instrument and related

104   individual products, provides 6-h, daily, and monthly wind and climate data with a spatial

105   resolution of $0.25°×0.25°$, and contains globally gridded ocean surface vector winds and wind

106   stresses (Zhang *et al*., 2006).

107   Sea surface temperature (SST) data are from remote-sensing systems (RSSs). The dataset

108   merges the near-coastal capability and high spatial resolution of infrared SST data with

109   through-cloud capabilities of microwave SST data, and has applied atmospheric corrections. It

110   provides daily data with a spatial resolution of 9 km×9 km from July 1, 2002 to the present.

111 2.2 Methods

112   2.2.1 Eddy energetic and hydrodynamic instability formula

113   The formation mechanisms of mesoscale eddies in the ocean are commonly attributed to

114 baroclinic and barotropic instabilities (Pedlosky, 1987). The barotropic conversion (BT) and

115 baroclinic conversion (BC) are manifestations of the baroclinic and barotropic instabilities,

116 respectively, and they are the major eddy energy sources around the LS (Yang *et al.,* 2013; Zhang

117 *et al.*, 2013, 2015, 2017). In addition, the wind-stress work (WW) can also contribute to the

118 formation of eddies (Ivchenko, 1997; Sun *et al.*, 2015). The BT, BC, and WW can be expressed as

119 follows (Ivchenko, 1997; Oey, 2008):

$$120 \qquad BT = -\int \left(\overline{u'^2} \frac{\partial \overline{u}}{\partial x} + \overline{v'^2} \frac{\partial \overline{v}}{\partial y} + \overline{u'v'} \frac{\partial \overline{u}}{\partial y} + \overline{u'v'} \frac{\partial \overline{v}}{\partial x} \right) dz, \qquad (1)$$

$$121 \qquad BC = -\int \frac{g^2}{\rho_0^2 N^2} \left(\overline{u'\rho'} \frac{\partial \overline{p}}{\partial x} + \overline{v'\rho'} \frac{\partial \overline{p}}{\partial y} \right) dz, \qquad (2)$$

$$122 \qquad WW = \frac{1}{\rho} \left(\overline{u'\tau'}_x + \overline{v'\tau'}_y \right), \qquad (3)$$

123 Where t is time; $u, v,$ and w are the zonal velocity, meridional velocity, and vertical velocity,

124 respectively, and their positive directions are east, north, and up, respectively. g is the

125 acceleration due to gravity; N is the buoyancy frequency; ρ is the density of sea water; $\rho_0 =$

126 $1030 \ kg \bullet m^{-3}$ is the mean sea-water density; p is the sea pressure; and τ_x and τ_y are the zonal

127 and meridional components of the wind stress, respectively. $x, y,$ and z are the conventional

128 east-west, north-south, and up-down Cartesian coordinates, respectively. The depth integrals for

129 BT and BC are from 400 m to the sea surface. The overbar denotes a time average over 70 d, the

130 primes denote deviations from the average value of 35 d before and after this day, and the other

131 symbols and notations are standard. From Figures 6 and 8, it can be seen that the counter-rotating

132 eddy-pair phenomenon occurs, develops, and disappears from t = −36 to t = 36, i.e., approximately

133 70 d. Therefore, the period is chosen to be 70 d. We have made several attempts to set the period

134 between 65 and 80 d, and they will not affect our basic conclusion. BT and BC were calculated

135 from HYCOM data. CMEMS surface-current velocity data and NCDC wind data were used to

136   calculate WW.

137   2.2.2 Vorticity budget equation

138   To examine the influence of the vorticity change, we applied the vorticity budget equation

139   (Muller,1995; Kuo and Tseng, 2021):

140
$$\frac{\partial \zeta}{\partial t} = -u\frac{\partial \zeta}{\partial x} - v\frac{\partial \zeta}{\partial y} - (\zeta + f)\nabla \bullet \vec{u} - v\frac{\partial f}{\partial y} + \frac{1}{\rho^2}\left(\frac{\partial \rho}{\partial x}\frac{\partial P}{\partial y} - \frac{\partial \rho}{\partial y}\frac{\partial P}{\partial x}\right) - v\frac{\partial^2 \zeta}{\partial^2 z}, \qquad (4)$$

141   Where $\zeta = \frac{\partial v}{\partial x} - \frac{\partial u}{\partial y}$ is the relative vorticity, t is time, f is the Coriolis parameter, P is the

142   sea-water pressure, and $v = 1.004 \times 10^{-6}$ is the kinematic viscosity coefficient.

143    $x, y, z, u, v,$ and ρ in formula (4) are as defined in formulas (1)-(3). The items on the right-hand

144   side of the equation are, from left to right, the zonal advection, meridional advection, stretching,

145   beta, baroclinic, and diffusion terms.

146   2.2.3 Definition of modes and intensity index of counter-rotating eddy-pair phenomenon

147   When an AE (a CE) in the NWP gradually approaches the northern LS, a CE (an AE)

148   gradually forms on the west side of the LS, and we define it as an AE (a CE) mode of the

149   counter-rotating eddy-pair phenomenon, as shown in Figures 2a, 3a, and 6 (Figures 2b, 3b, and 8).

150   To reflect the intensity of counter-rotating eddy-pair phenomenon, we must construct an

151   intensity index. As this phenomenon mainly involves the difference of SSHA between the east and

152   west sides of the LS, the index is defined as the time series of the SSHA in the east red box of

153   Figure 2 (expressed as $SSHA_{east}$) minus that in the west red box of Figure 2 (expressed as $SSHA_{west}$),

154   which is shown in Figure 3a and can be expressed as $Index = SSHA_{east} - SSHA_{west}$.

155   **3 Results**

156   3.1 Identification of counter-rotating eddy pair in LS

157   Based on cluster analysis, which is the same as the clustering method used by Sun *et al.*

158   (2018), the SSHA and sea-temperature anomaly (STA) are determined based on the days when an

159   AE and a CE exist on the east side of the LS (shown in the white box in Figure 1), respectively.

160   Figure 2a shows that the SSHA in the red box on the east side of the LS increases from the outside

161   to inside, which means that there is an AE. Owing to geostrophic balance and mass conservation,

162   the AE causes convergence of sea water, leading to down-welling in its center, subsequently

163   leading to an increase in the temperature in the deep ocean. This is verified by the fact that the

164   STA in the red box on the east side of the LS gradually increases from outside to inside and the

165   value is highest in the center. In addition, the SSHA in the red box on the west side of the LS

166   decreases from outside to inside and the STA is negative, indicating the presence of a weak CE.

167   According to the definition of modes of the counter-rotating eddy pair given in Section 2.2.3, the

168   SSHA pattern in Figure 2a can be identified as an AE mode of the counter-rotating eddy pair.

169   Figure 2b is similar to Figure 2a, but for a CE and an AE on the east and west sides of the LS,

170   respectively, its SSHA pattern can be identified as an AE mode of the counter-rotating eddy pair.

171   According to the intensity index defined in Section 2.2.3, the SSHA is constructed based on the

172   days when the positive and negative intensity index values are more than one standard deviation

173   from the mean, as shown in Figures 3b and 3c. Figure 3b (3c) shows that an AE (a CE) on the east

174   side of the LS corresponds well to a CE (an AE) on the west side of the LS, and can well reflect

175   the AE (CE) mode of a counter-rotating eddy pair in the LS. It also shows that we can well

176   identify this phenomenon according to the intensity index, and, furthermore, that the positive and

177   negative intensity indexes correspond to AE and CE modes, respectively, of this phenomenon.
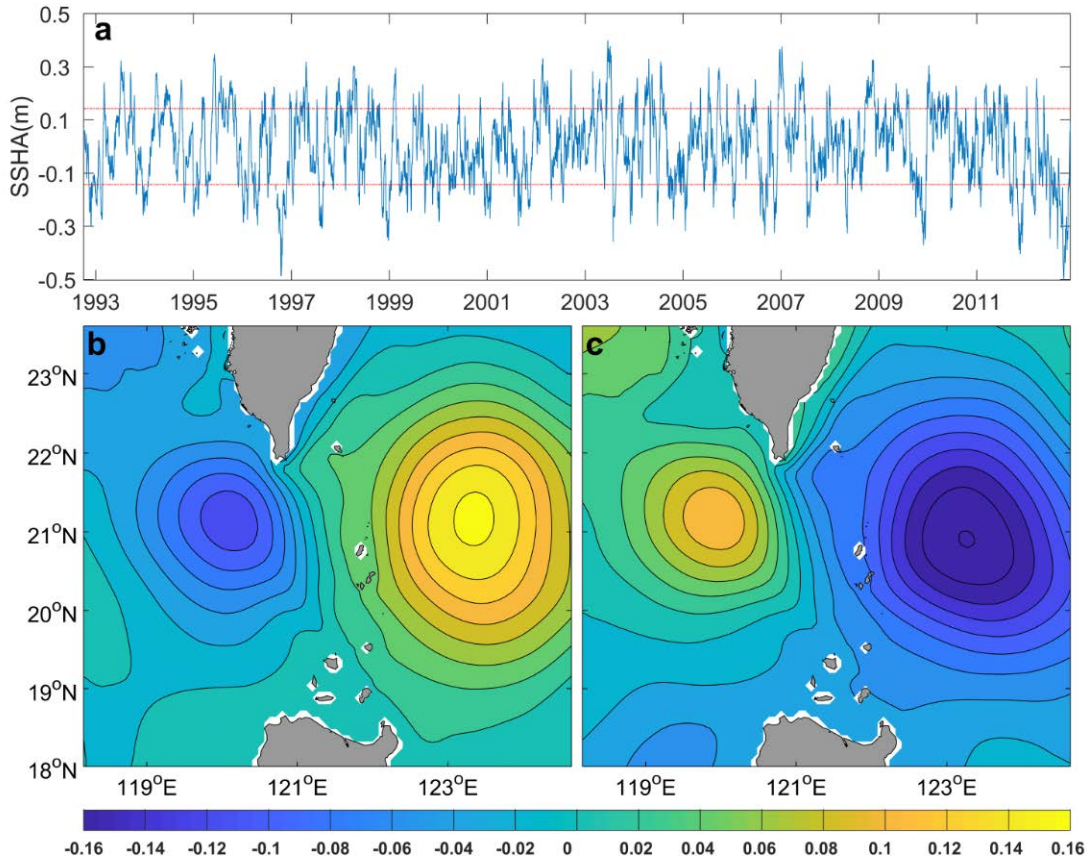
Figure 3. Time series of intensity index of counter-rotating eddy pair in LS (a). Red dotted line

above (below) represents the sum (difference) of one time the standard deviation and the average

value of the time series. Composition of SSHA for positive (b) and negative (c) intensity-index

days. SSHA interval is 0.02 m. Figure based on HYCOM data.

3.2 Seasonal variation of counter-rotating eddy pair in LS

We counted the temporal distribution of the positive and negative intensity index values in a

statistical sense. Figure 4a (4b) shows that most of the AE (CE) mode of the instances of the

counter-rotating eddy pair occur in the summer (winter) half of the year. The first two months with

the highest incidences of the AE (CE) mode are May and June (December and January), and their

occurrence rates are 17.01% and 15.47% (19.69% and 15.57%), respectively. We constructed the

geostrophic current in May and June (Figure 5a) and in December and January (Figure 5b). The

patterns of the Kuroshio Current in Figures 5a and 5b exhibit as the "Leap" and "Loop" patterns

191   of the Kuroshio in the LS, which illustrates that the Leap and Loop patterns of the Kuroshio

192   contribute to the occurrence of the AE and CE modes, respectively, of the counter-rotating eddy

193   pair. Figure 5c (5d) shows that the geostrophic current anomaly in the northern LS is northward

194   (southward). It produces positive (negative) vorticity through horizontal velocity shear on the west

195   side of the LS, and then contributes to the formation of a CE (an AE) on the west side of the LS.

196   We discuss the dynamic mechanism of the counter-rotating eddy-pair phenomenon in detail in

197   Section 3.3.
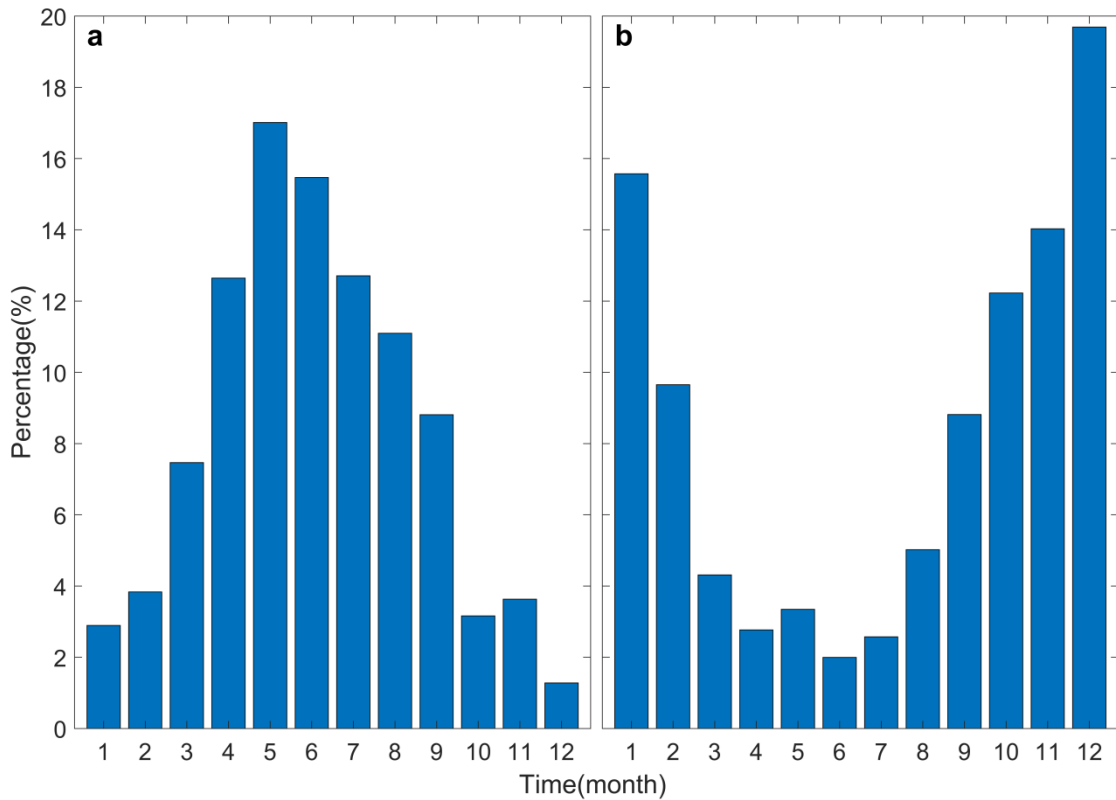
198

199   Figure 4. Seasonal distribution of occurrence rate for positive (a) and negative (b) intensity

200   indexes.
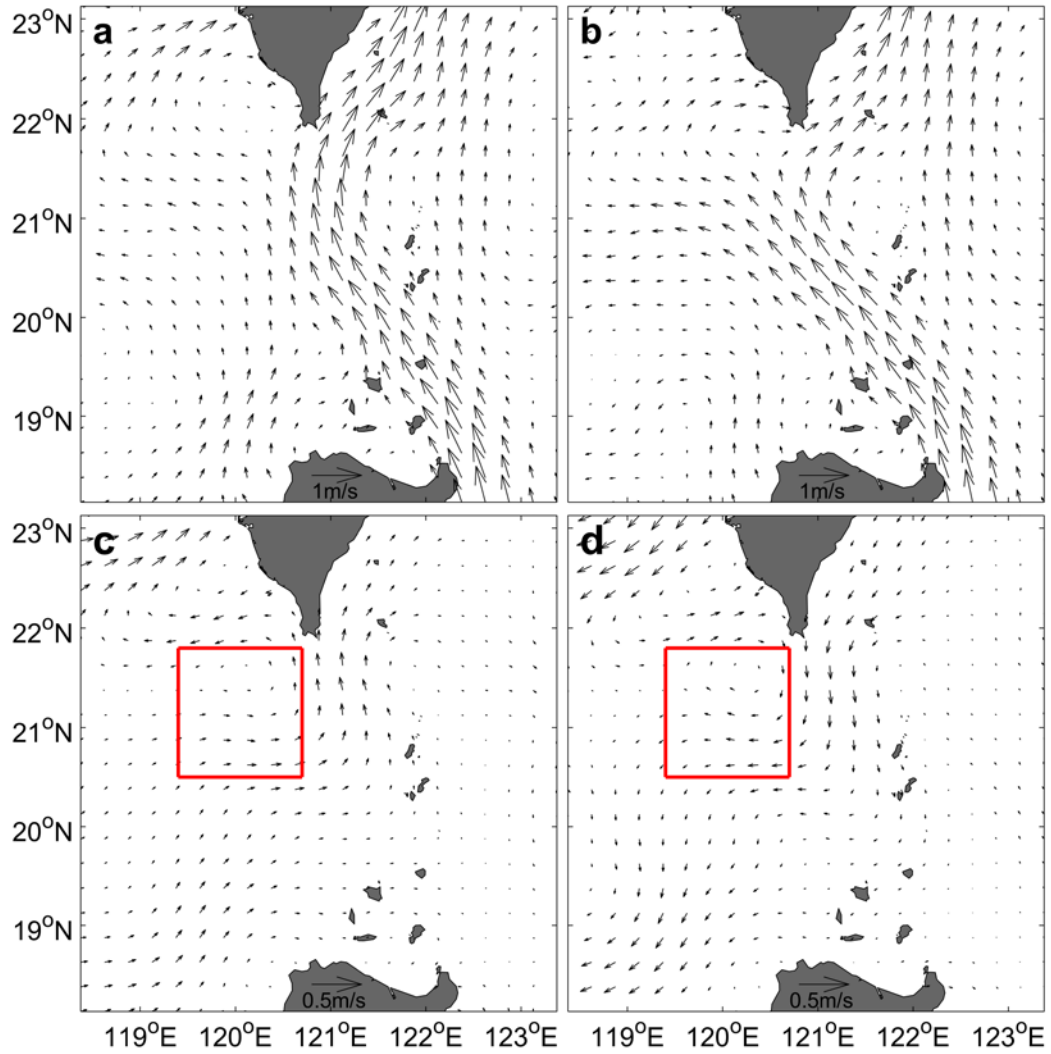
201

202 Figure 5. Climatic distributions of geostrophic current in May and June (a) and in December and

203 January (b), and of geostrophic current anomaly in May and June (c) and in December and

204 January (d). Red boxes in c and d outline 20.5–21.8°N, 119.4–120.7°E, which represent the

205 position of mesoscale eddies on west side of LS. Figure based on CMEMS data.

206 3.3 Evolution of counter-rotating eddy pair in LS

207 Figure 6 shows the spatial evolution of the AE mode of the counter-rotating eddy pair in the

208 LS. It shows that at the beginning, for example, at t = −24, there is a weak AE far from the east

209 side of the LS, but no CE on the west side of the LS. From t = −20 to t = 0, as the AE in the NWP

210 approaches the northern LS, a CE gradually forms on the west side of the LS. At t = 0, the AE

211   mode reaches its maximum. Then, from t = 4 to t = 36, as the AE in the NWP gradually moves

212   away from the northern LS, the CE on the west side of the LS gradually weakens until it finally

213   dies out.

214   The growth and weakening of a mesoscale eddy must be accompanied by a change in its

215   relative vorticity. Figure 7a shows that as the AE on the east side of the LS approaches and then

216   moves away from the northern LS, its relative vorticity initially decreases and then increases,

217   while the relative vorticity of the corresponding CE on the west side of the LS initially increases

218   and then decreases. The maximum negative (positive) value of the time series of the AE (CE) on

219   the east (west) side of the LS reaches -4.2×10^{-6} s^{-1} (3.6×10^{-6} s^{-1}). These time series have good

220   correspondence and their correlation coefficient is -0.97 at the 95% confidence level. Therefore,

221   the temporal variations in the relative vorticity in Figure 7a verify the evolution of the AE mode of

222   the counter-rotating eddy pair in the LS.

223
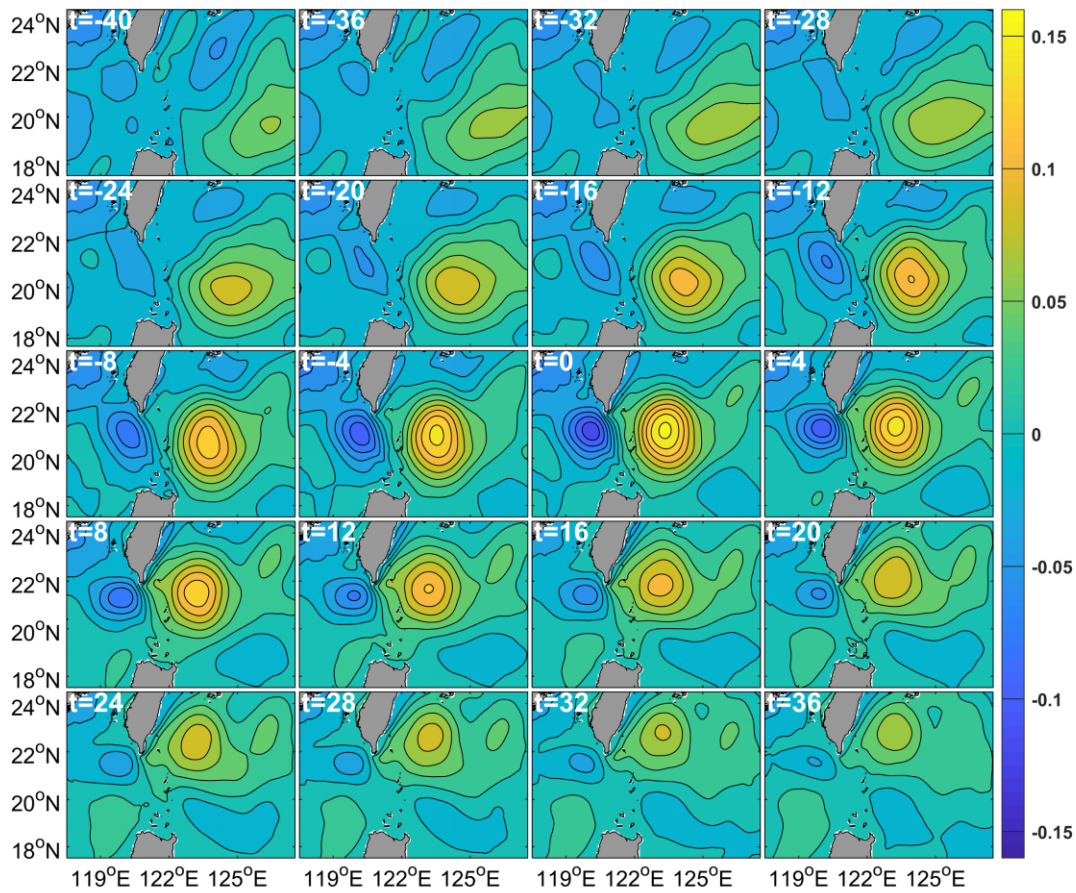
Figure 6. Evolution of AE mode of counter-rotating eddy pair in LS based on HYCOM data.

Contours and shading both represent SSHA (units of m). SSHA interval is 0.02 m. t value in the

top left-hand corner of each panel denotes the days before (negative value) or after (positive value)

AE mode of counter-rotating eddy pair reached the maximum (t=0). t = 0 corresponds to the time

of Figure 3b.

229
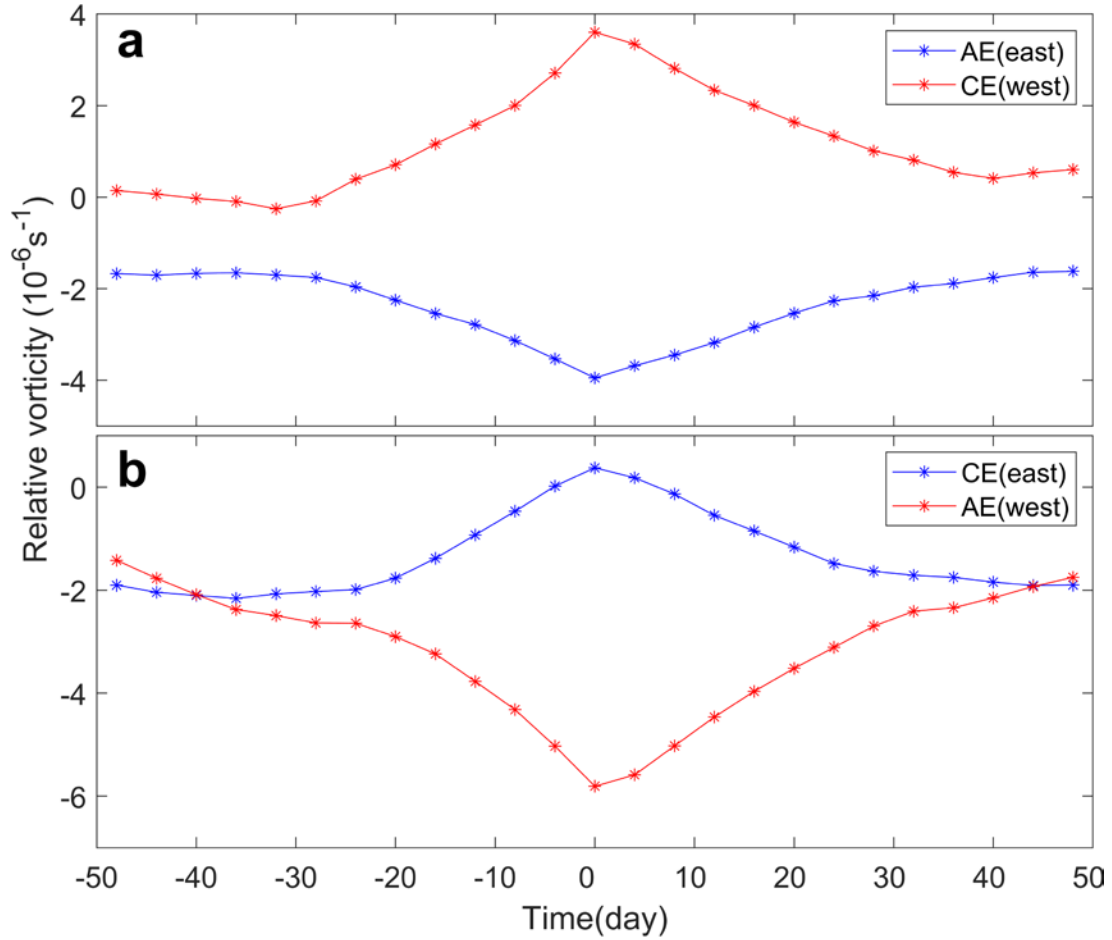
Figure 7. Distribution of relative vorticity in area bordered by red boxes in Figure 2. Panel a,

relative vorticity of AE mode over time. Blue (red) line represents time series of relative vorticity

of AE (CE) on east (west) side of LS, which corresponds to Figure 6. Panel b, relative vorticity of

CE mode over time. Blue (red) line represents time series of relative vorticity of CE (AE) on east

(west) side of LS, which corresponds to Figure 8. Figure based on HYCOM data.

Figure 8 plots the CE mode of the counter-rotating eddy pair in the LS. It shows that at the

beginning, for example, at t = −32, there is a weak CE far from the east side of the LS, but no AE

on the west side of the LS. From t = −28 to t = 0, as the CE in NWP approaches the northern LS,

an AE gradually forms on the west side of the LS. At t = 0, the CE mode of the evolution of the

counter-rotating eddy pair reaches the maximum. Then, from t = 4 to t = 36, as the CE in the NWP

240 gradually moves away from the northern LS, the AE in the west side of the LS gradually weakens

241 until it finally dies out. Figure 7b plots the CE mode and shows that as the CE on the east side of

242 the LS approaches and moves away from the northern LS, its relative vorticity initially increases

243 and then decreases, while the relative vorticity of the corresponding AE on the west side of the LS

244 initially decreases and then increases. The maximum positive (negative) value of the time series of

245 the CE (AE) on the east (west) side of the LS can reach $0.48 \times 10^{-6}\,\mathrm{s}^{-1}$ ($-6.7 \times 10^{-6}\,\mathrm{s}^{-1}$). These time

246 series have good correspondence and their correlation coefficient is -0.96 at the 95% confidence

247 level. Therefore, the temporal variations in the relative vorticity in Figure 7b verify the evolution

248 of the AE mode of the counter-rotating eddy pair in the LS. The evolution of the AE and CE

249 modes of the counter-rotating eddy pair in the LS is also reflected by the satellite observations

250 (Figures 9 and 10).

251

252

253

254
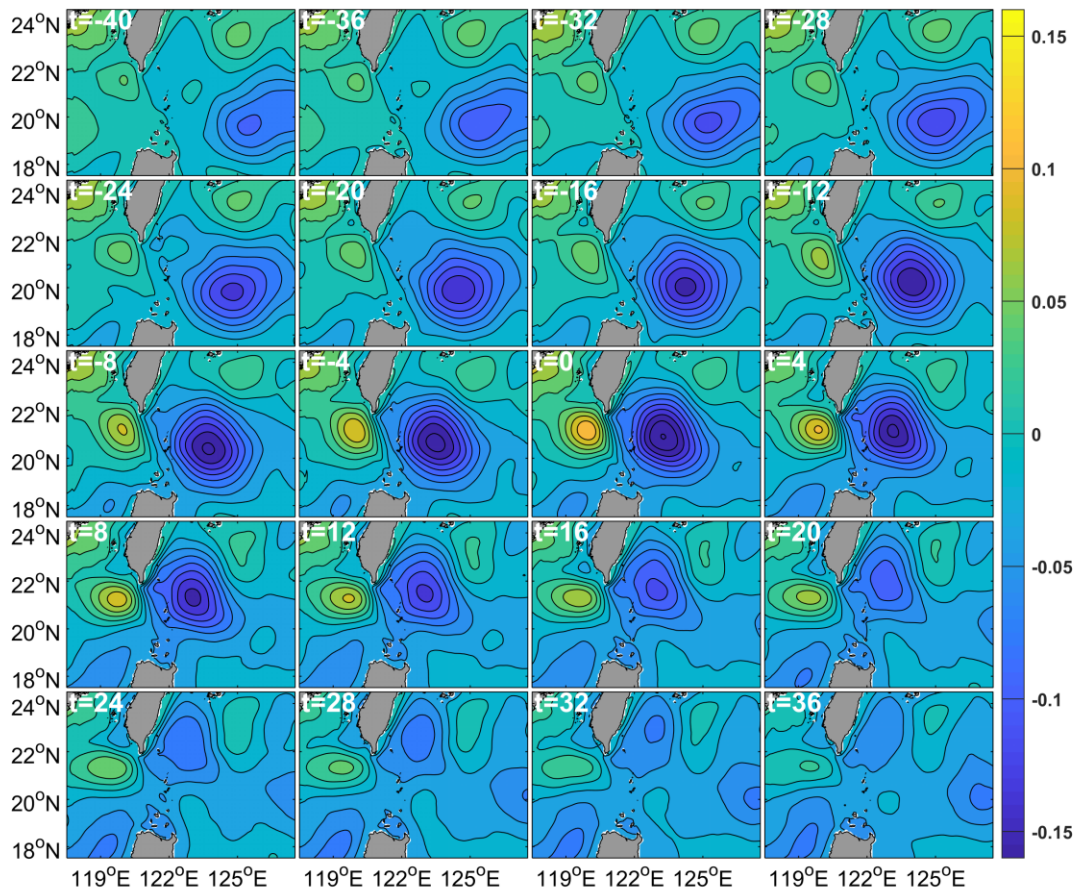
Figure 8 Evolution of CE mode of counter-rotating eddy pair in LS based on HYCOM data.

Contours and shading both represent SSHA (units of m). SSHA interval is 0.02 m. t in the top

left-hand corner of each panel denotes the days before (negative value) or after (positive value) the

CE mode of the counter-rotating eddy pair reached the maximum (t=0). t = 0 corresponds to time

of Figure 3b.

260

261
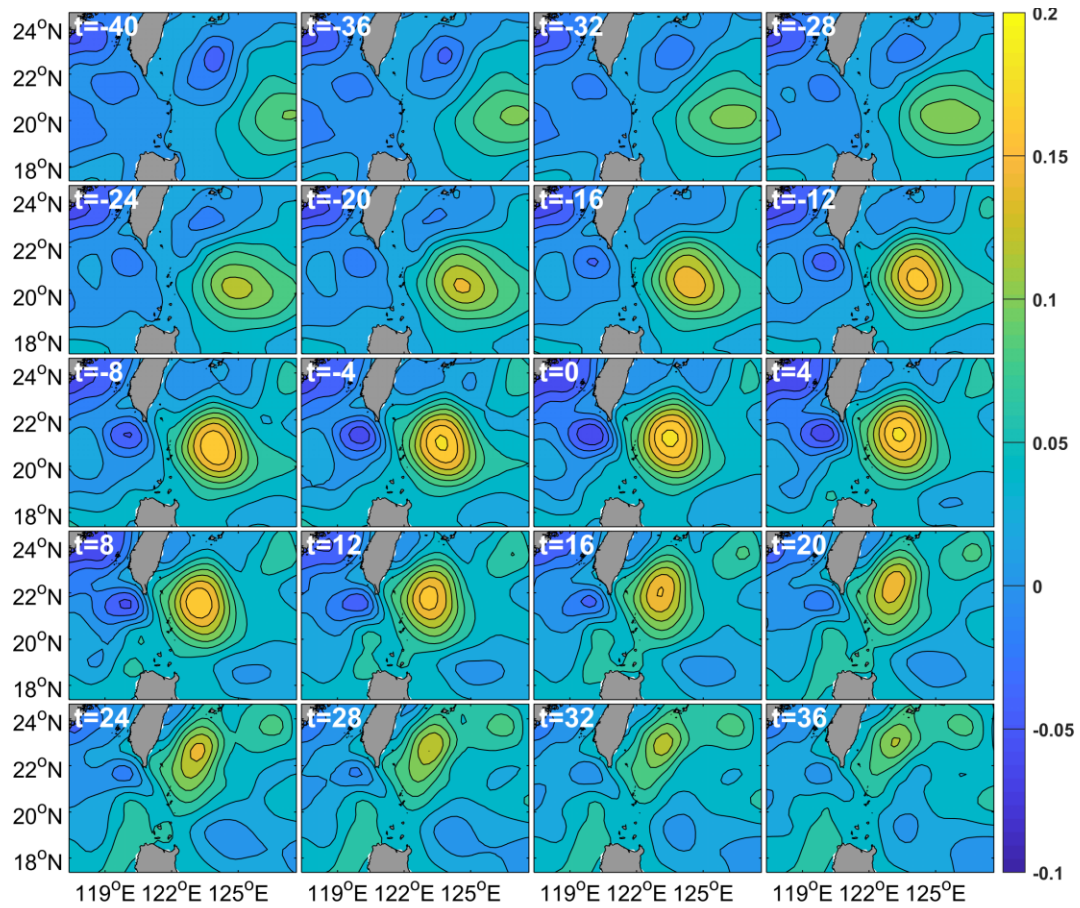
262

263 Figure 9 Evolution of AE mode of counter-rotating eddy pair in LS based on CMEMS data.

264 Contours and shading both represent SSHA (units of m). SSHA interval is 0.02 m. t in the top

265 left-hand corner of each panel denotes days before (negative value) or after (positive value) the

266 AE mode of counter-rotating eddy pair reached the maximum (t=0). t = 0 corresponds to time of

267 Figure 3b.

268

269

270
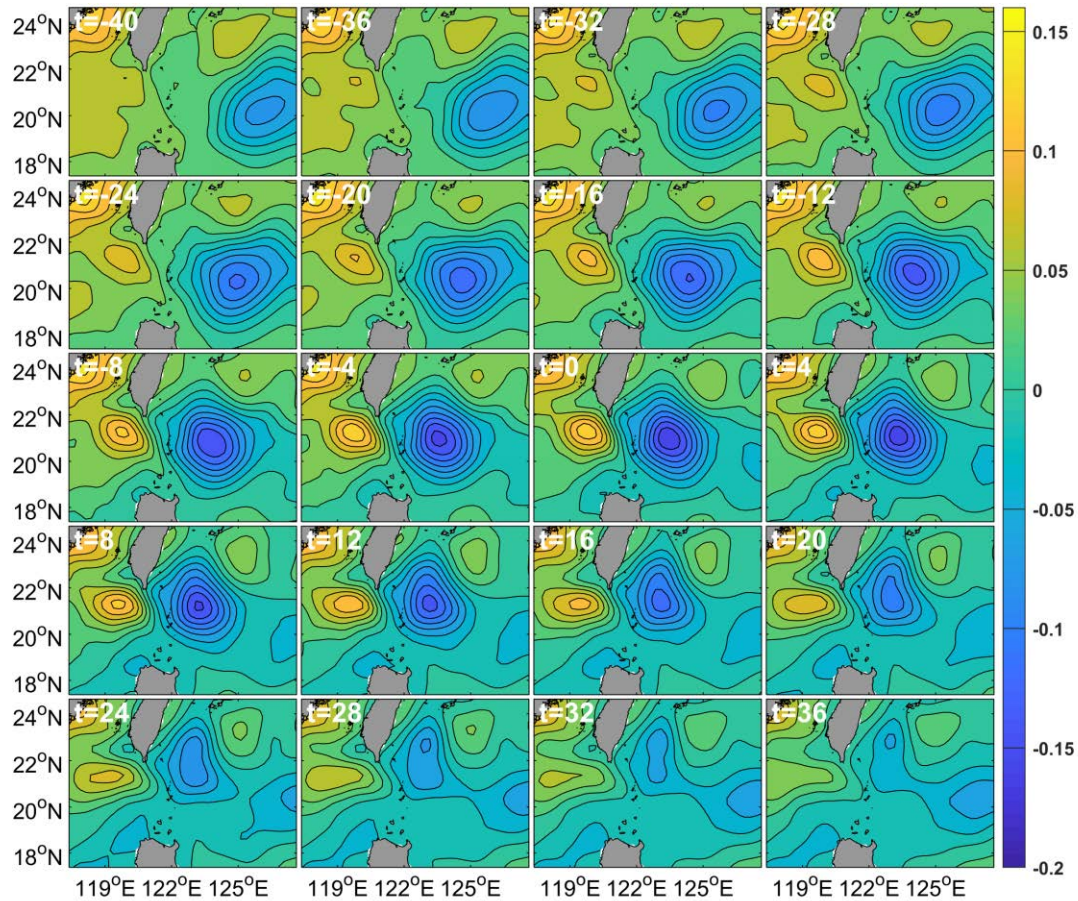
271

272 Figure 10 Evolution of CE mode of counter-rotating eddy pair in LS based on CMEMS data.

273 Contours and shading both represent SSHA (units of m). SSHA interval is 0.02 m. t in the top

274 left-hand corner of each panel denotes days before (negative value) or after (positive value) the

275 CE mode of counter-rotating eddy pair reached the maximum (t=0). t = 0 corresponds to time of

276 Figure 3b.

277 3.4 Formation mechanism of counter-rotating eddy pair in LS

278   Zhang *et al*. (2017) reported that CEs mainly formed due to the barotropic instability caused

279 by horizontal velocity shear of the Kuroshio Loop current southwest of Taiwan Island. Huang *et al*.

280 (2019) discovered that an AE from the NWP caused a CE to form on the west side of the LS via

281 horizontal velocity shear. In addition, Figures 3b and 3c show that the dense contour of the SSHA

282 means that there are strong current anomalies and thus strong horizontal velocity shear at the

283   junction of the AE and CE. Therefore, we investigated the role of horizontal velocity shear in the

284   formation of a counter-rotating eddy in the LS.

285   Because meridional horizontal velocity shear is weak, we only show the zonal velocity shear.

286   Figure 11 shows that from t = −40 to t = 0, as the AE on the east side of the NWP gradually

287   approaches the northern LS, the absolute value of the zonal horizontal velocity shear ($\frac{\partial v}{\partial x}$)

288   gradually increases, and a CE gradually forms and strengthens on the west side of the LS. From t

289   = 0 to t = 36, as the AE gradually moves away from the northern LS, the absolute value of the

290   zonal horizontal velocity shear gradually decreases, and the CE on the west side of the LS

291   gradually weakens. Figure 12 plots the CE mode of the counter-rotating eddy pair in the LS and

292   shows a similar corresponding evolution process. This demonstrates that there is good

293   correspondence between the zonal horizontal velocity shear and evolution process of the

294   counter-rotating eddy pair.
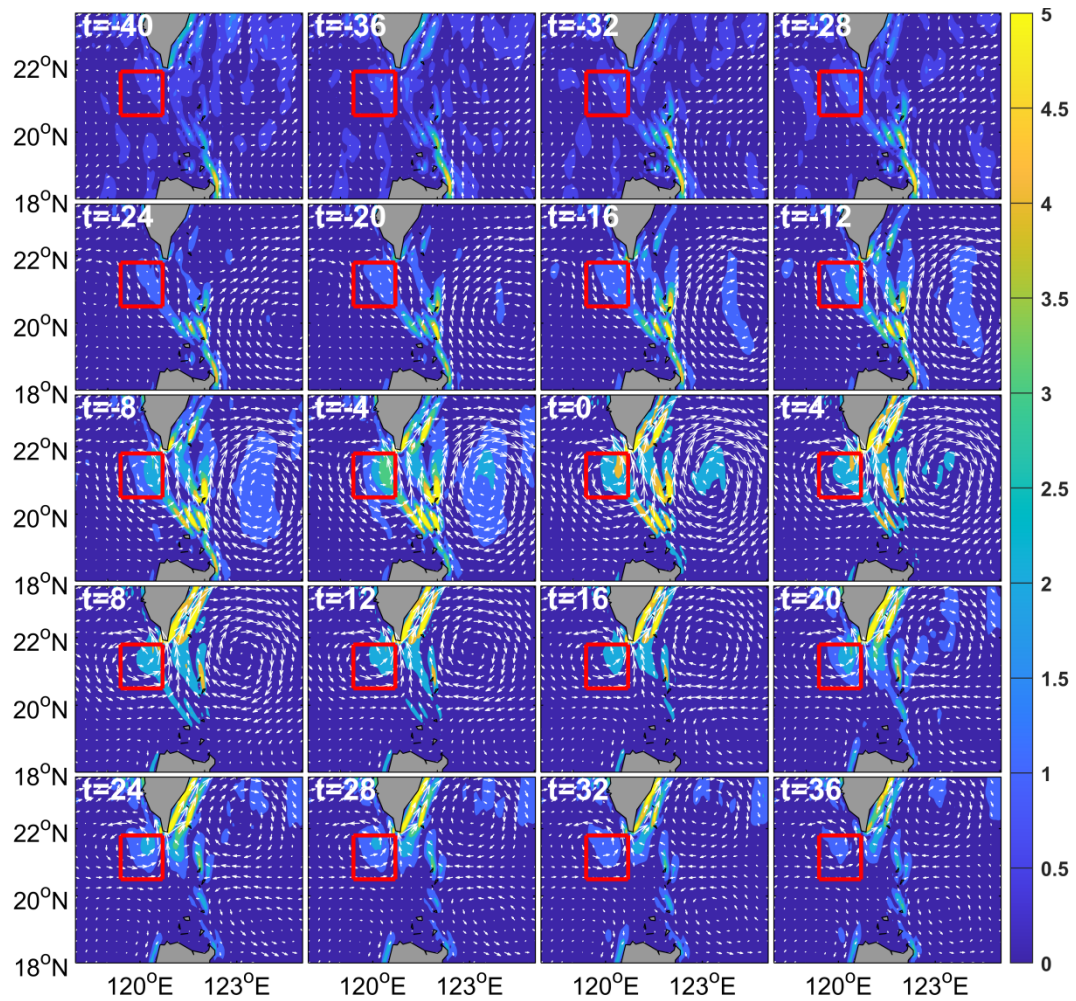
Figure 11 Evolution process of absolute value of zonal horizontal velocity shear ($\frac{\partial v}{\partial x}$) for AE

mode of counter-rotating eddy pair in LS based on HYCOM data. Shading represents zonal

horizontal velocity shear (units of $10^{-6}\,\mathrm{s}^{-2}$). Vector represents the current anomaly. t in the top

left-hand corner of each panel denotes days before (negative value) or after (positive value) the

AE mode of counter-rotating eddy pair reached the maximum (t = 0). t = 0 corresponds to time of

Figure 3b. Red boxes on west side of LS cover 20.5–21.8°N, 119.4–120.7°E and represent

location of CE on west side of LS.
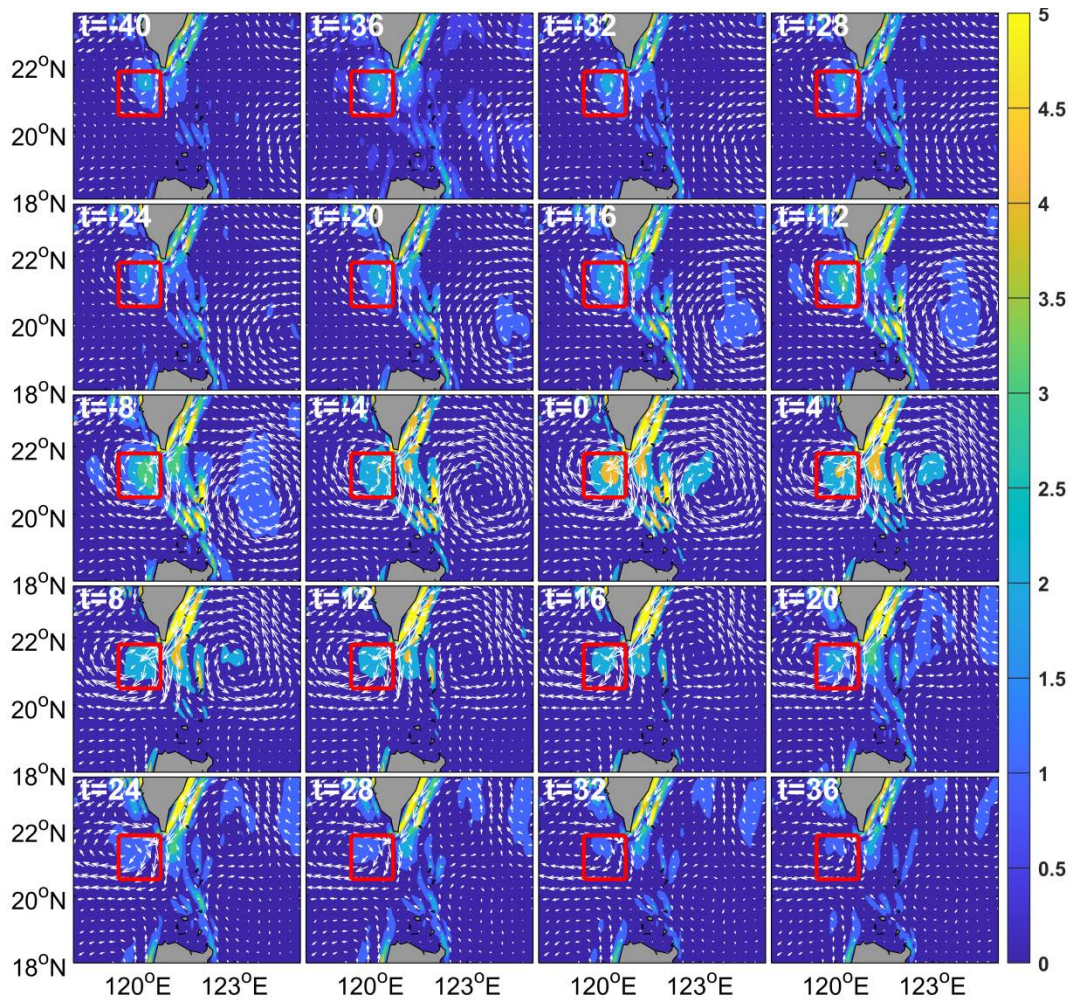
303

304 Figure 12 Evolution process of absolute value of zonal horizontal velocity shear ($\frac{\partial v}{\partial x}$) for CE

305 mode of counter-rotating eddy pair in LS based on HYCOM data. Shading represents zonal

306 horizontal velocity shear (units of $10^{-6}\,\mathrm{s}^{-2}$). Vector represents current anomaly. t in top left-hand

307 corner of each panel denotes days before (negative value) or after (positive value) the AE mode of

308 counter-rotating eddy pair reached the maximum (t = 0). Time t = 0 corresponds to time of Figure

309 3b. Red boxes on west side of LS cover 20.5-21.8°N, 119.4-120.7°E and represent the location of

310 CE on west side of LS.

311   However, Figure 11 (12) shows that zonal horizontal velocity shear only occurs on the

312 right-hand side of the red box; that is, on the right-hand side of the CE (AE). How does the

313 horizontal velocity shear pass to the entire CE (AE)? To answer this question, we used the

314 vorticity budget equation. Figures 13a1–f1 plot the AE mode of the counter-rotating eddy pair and

315 show the respective contributions of the zonal advection, meridional advection, stretching, beta,

316 baroclinic, and diffusion terms of the vorticity budget equation. Compared to the stretching, beta,

317 baroclinic, and diffusion terms, the values of the zonal advection and meridional advection terms

318 in the red box are large. However, most of the values of the meridional advection term in the red

319 box are negative. Only positive vorticity advection can lead to formation of a CE, which suggests

320 that the zonal advection term is the main cause of CE formation in the red box. To further test this

321 conclusion, Figure 14a shows the correspondence between the relative vorticity anomaly and

322 zonal advection of the vorticity in the red box in Figure 13, illustrating that there is good

323 correspondence and their correlation coefficient is as high as 0.96 at the 95% confidence level.

324 Therefore, we conclude that the zonal advection term plays the most important role in vorticity

325 transport and contributes to the formation of the CE on the west side of the LS.

326   Figures 13a2–f2 are plots the CE mode of the counter-rotating eddy pair and shows that,

327 compared to the stretching, beta, baroclinic, and diffusion terms, the values of the zonal advection

328 and meridional advection terms in the red box are large. However, most of the values of the

329 meridional advection term in the red box are positive. Only negative vorticity advection can lead

330 to formation of an AE, which implies that the zonal advection term is the main cause of AE

331 formation in the red box. To further test this conclusion, Figure 14b shows the correspondence

332 between the relative vorticity anomaly and zonal advection of vorticity, illustrating that there is

333 good correspondence and their correlation coefficient is as high as 0.84 at the 95% confidence

334 level. Therefore, we conclude that the zonal advection term plays the most important role in

335 vorticity transport and contributes to the formation of the AE on the west side of the LS.
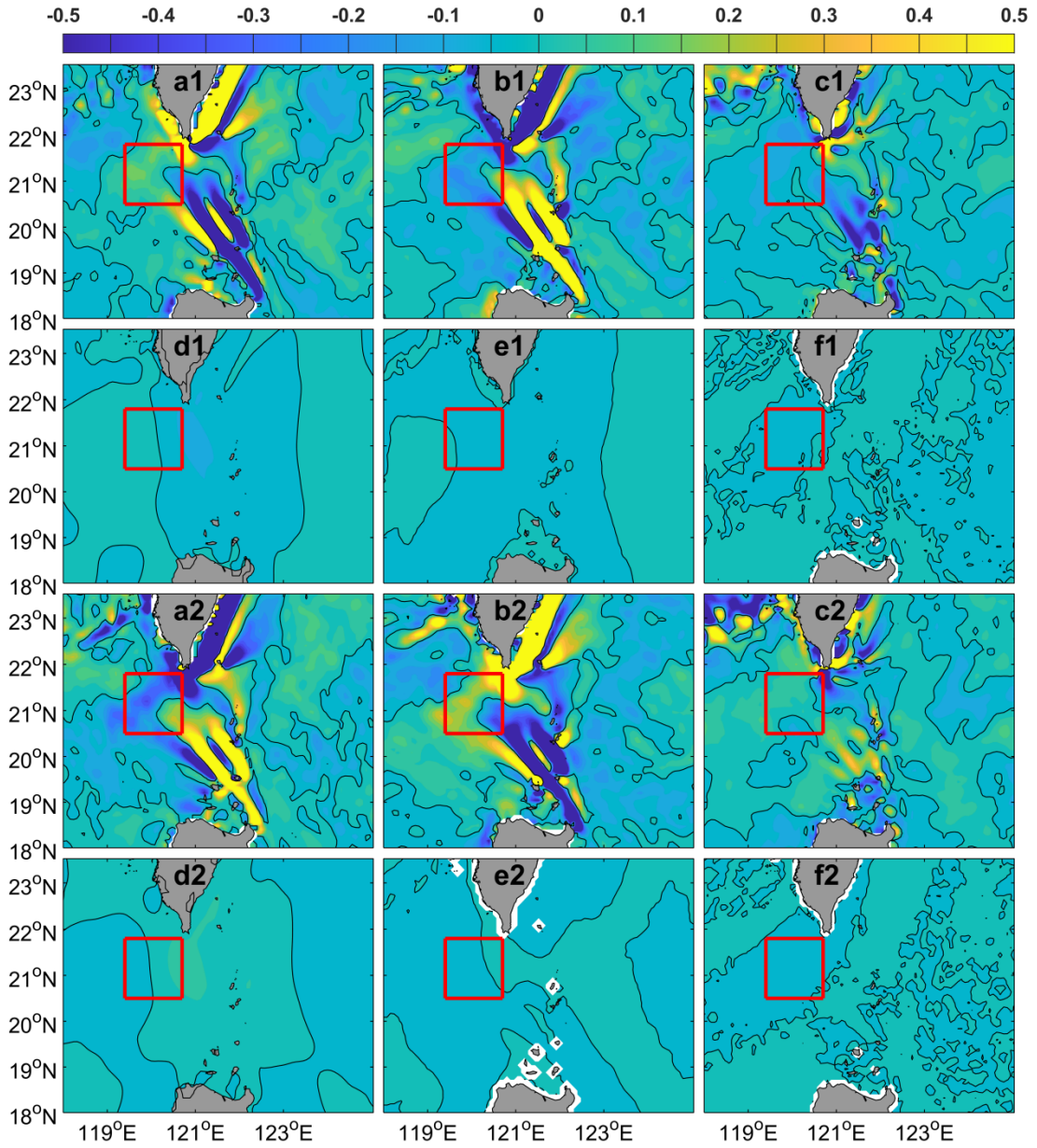
Figure 13. Vorticity budget equation for (a1–f1) AE mode of counter-rotating eddy pair and (a2–f2) CE mode of counter-rotating eddy pair. a1 and a2 represent the zonal advection term, b1 and b2 the meridional advection term, c1 and c2 the stretching term, d1 and d2 the beta term, e1 and e2 the baroclinic term, and f1 and f2 the diffusion term. Units are $10^{-10}\,\text{s}^{-2}$. Red boxes on west side of LS border cover 20.5–21.8°N, 119.4–120.7°E, and represent location of CE or AE on west side of LS. Black solid line represents the zero contour. Figure based on HYCOM data.
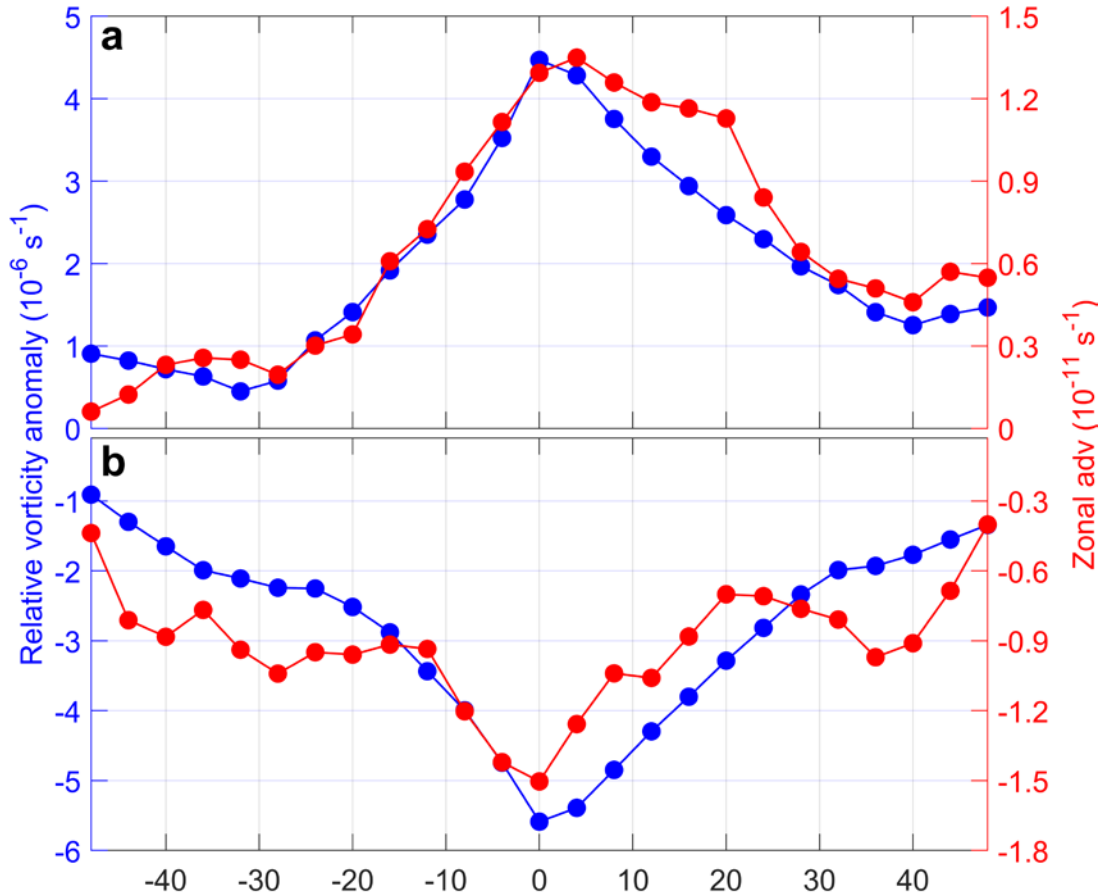
343

344   Figure 14. Distribution of relative vorticity anomaly and zonal advection of vorticity

345   surrounded by red boxes in Figure 13 for AE (a) and CE (b) modes of counter-rotating eddy pair

346   in LS.

347   We proposed above that the horizontal velocity shear caused by the mesoscale eddy on the east

348   side of the LS is transported westward through zonal advection, resulting in the formation of a

349   counter-rotating mesoscale eddy on the west side of the LS. Horizontal velocity shear will

350   inevitably lead to barotropic instability. Now, we verify our conclusion from the perspective of

351   energy. Figures 15a, 15b, and 15c show that, compared to the BC and WW values, the BT values

352   in the LS are large and most of the values are positive, especially in the area surrounded by the red

353   box in Figure 15a, which is the junction of the AE and CE. This means that the BT plays the most

354   important role in formation of the AE on the west side of the LS.

355   Figures 15d, 15e, and 15f show the BT, BC, and WW, respectively, corresponding to the AE

356   mode of the counter-rotating eddy pair in the LS. The description and dynamic mechanism of the

357   AE mode are similar to those of the CE mode of the counter-rotating eddy pair in the LS, so the

358   details will not be discussed here.

359
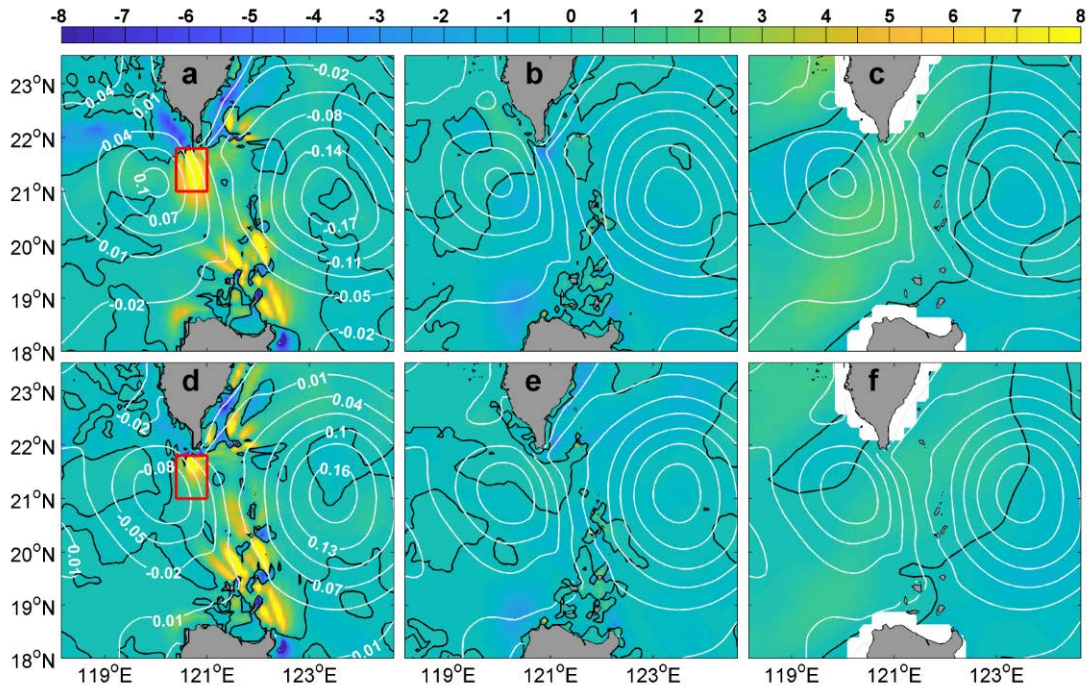
360   Figure 15. BT based on HYCOM data (10^{-5} m^3 s^{-3}) represented by colors (a, d); BC based on

361   HYCOM data (10^{-5} m^3 s^{-3}) represented by colors (b, e); WW based on CMEMS surface velocity

362   data and NCDC wind data (10^{-5} m^3 s^{-3}) represented by colors (c, f). Red box borders 21°N–

363   21.8°N, 120.4°E–121°E. White contours represent SSHA contours of. Panels a, b, and c (d, e, and

364   f) plot CE (AE) mode of counter-rotating eddy pair in LS.

365   **4 Discussion and conclusions**

366   In this study, based on satellite observation data and HYCOM re-analysis data, the

367   counter-rotating eddy pair in the LS is investigated. The phenomenon of counter-rotating eddy

368   pairs is defined as the stage when an AE (a CE) in the NWP gradually approaches the northern LS,

369   and a CE (an AE) forms on the west side of the LS. This phenomenon exhibits obvious seasonal

370 variation; that is, the AE mode mainly occurs in the summer half of the year, while the CE mode

371 mainly occurs in the winter half of the year. The mean durations of the AE and CE modes are both

372 approximately 70 d. The Leap and Loop patterns of the Kuroshio Current contribute to the

373 occurrence of the AE and CE modes, respectively, of counter-rotating eddy pairs. Based on the

374 vorticity budget equation and energy analysis, the dynamic mechanism of the occurrence of a

375 counter-rotating eddy pair is as follows. The AE (CE) in the NWP causes a positive (negative)

376 vorticity anomaly through horizontal velocity shear on the west side of the LS, and the positive

377 (negative) vorticity anomaly is transported westward by the zonal advection of the vorticity,

378 finally leading to the formation of a CE (an AE) on the west side of the LS. This conclusion is also

379 verified by barotropic instability based on the energy analysis.

380 When we investigated the question of how the horizontal velocity shear passes to the entire

381 CE or AE in Section 3.4, we found that the magnitudes of the meridional and zonal advection

382 terms are roughly the same. Because the meridional advection term has the opposite effect of CE

383 (AE) formation in the west side of the LS for the AE (CE) mode of the counter-rotating eddy pair,

384 we confirmed that the zonal advection term plays a main role in horizontal velocity shear

385 transportation. However, since the magnitude of the meridional advection term is very large, it

386 may play a role in the ocean dynamic process of the LS, which deserves further study.

387 The results presented in this study are preliminary and several problems require further

388 research. The occurrence probability of a counter-rotating eddy pair in the LS must be determined.

389 The counter-rotating eddy pair phenomenon involves spatiotemporal variations in two mesoscale

390 eddies on both sides of the LS, and it is difficult to provide a quantifiable definition of this

391 phenomenon for a single event. For example, how far apart must the mesoscale eddies on the east

392   and west sides of the LS be to define them as a counter-rotating eddy pair. We preliminarily

393   calculated that the incidence of this phenomenon is approximately 5%.

394   Another problem to solve involves threshold of the NWP mesoscale eddies entering the SCS,

395   and what role the Kuroshio Current plays in the counter-rotating eddy-pair phenomenon in the LS.

396   In this study, our illustration of the counter-rotating eddy pair phenomenon does not include the

397   mean current field, which means that the influence of the Kuroshio Current is not considered.

398   However, the role of the Kuroshio in energy transfer is still worthy of further study. Numerical

399   simulations can be useful to address this issue. Our study provides new perspective on particle and

400   energy exchange, and further perfects the theory of particle and energy exchange between the SCS

401   and NWP.

402

403   **Acknowledges**

404   The authors would like to acknowledge several data sets used in this paper. Satellite remote

405   sensing geostrophic current data and sea level anomaly were obtained from the CMEMS, the

406   HYCOM reanalysis data were downloaded from HYCOM organization, the data set of wind was

407   provided by National Climate Data Center. Sea surface temperature data comes from Remote

408   Sensing System. This study was supported by National Natural Science Foundation of China

409   (grant number 41806019), National Key R&D Program of China (2019YFD0901305), Key R&D

410   projection of Zhejiang Province (2020C03012), National Natural Science Foundation of China

411   (No.41776012), State Key Laboratory of Tropical Oceanography (South China Sea Institute of

412   Oceanology Chinese Academy of Sciences) open topics (grant number LTO2011), Key R&D

413   project of Guangdong Province (2020B1111030002), Major science and technology project of

Sanya YZBSTC (SKJC-KJ-2019KY03). We thank LetPub (www.letpub.com) for its linguistic

assistance during the preparation of this manuscript.

Reference

Huang Z, Zhuang W, Hu J, et al. Observations of the Luzon Cold Eddy in the northeastern South China Sea in May 2017[J]. Journal of Oceanography,2019, 75(5): 415-422.

Jing C, Li L. An initial note on quasi-stationary, cold-core Lanyu eddies southeast off Taiwan Island[J]. Chinese Science Bulletin. 48(19): 2101-2107.

Kuo Y, Tseng Y. Influence of anomalous low-level circulation on the Kuroshio in the Luzon Strait during ENSO[J]. Ocean Modelling, 2021, 159, 101559.

Ivchenko V O, Treguier A M, and Best S E. A kinetic energy budget and internal instabilities in the fine resolution antarctic model, Journal of Physical Oceanography, 1997, 27:5-22.

Liu Y, Dong C, Guan Y, et al. Eddy Analysis in the Subtropical Zonal Band of the North Pacific Ocean[J]. Deep Sea Research Part I, 2012, 68:54-67.

Lu J, Liu Q. Gap-leaping Kuroshio and blocking westward-propagating Rossby wave and eddy in the Luzon Strait[J]. Journal of Geophysical Research Oceans, 2013, 118(3):1170-1181.

Muller P. Ertel's potential vorticity theorem in physical oceanography[J]. Reviews of Geophysics, 1995, 33(1):67-97.

Oey L Y. Loop Current and Deep Eddies[J]. Journal of Physical Oceanography, 2008, 38(7): 1426 -1449.

Pedlosky J. Geophysical Fluid Dynamics, 1987, 2nd ed., 710 pp., Springer, N. Y.

Pujol M, Francoise M. Product user manual for sea level SLA products. Copernicus Monitoring Environment Marine Service (CMEMS), 2022, https://doi.org/10.48670/moi-00148.

Remote Sensing Systems (RSS): https://www.remss.com/measurements/ sea-surface-temperature/.

438   Sun R, Ling Z, Chen C, et al. Interannual variability of thermal front west of Luzon Island in

439   boreal winter[J]. Acta Oceanologica Sinica, 2015, (34):108.

440   Sun R, Wang G, Chen C. The Kuroshio bifurcation associated with islands at the Luzon Strait[J].

441   Geophysical Research Letters, 2016a, 43(11):5768-5774.

442   Sun R, Gu Y, Li P, et al. Statistical characteristics and formation mechanism of the Lanyu cold

443   eddy[J]. Journal of Oceanography, 2016b, 72(4):641-649.

444   Sun R, Zhai F, Gu Y. The Four Patterns of the East Branch of the Kuroshio Bifurcation in the

445   Luzon Strait[J]. Water, 2018, 10(12).

446   Sun R, Zhai F, Zhang G, et al. Cold Water in the Lee of the Batanes Islands in the Luzon Strait[J].

447   Journal of Ocean University of China, 2020, 19(6):10.

448   Wallcraft A, Carroll S N, Kelly K A, et al. Hybrid Coordinate Ocean Model (HYCOM) Version

449   2.1 User's Guide. HYCOM consortium, 2003. Https://www.hycom.org/dataserver/gofs-3pt0

450   /reanalysis.

451   Yang H, Wu L, Liu H, et al. Eddy energy sources and sinks in the South China Sea[J]. Journal of

452   Geophysical Research Oceans, 2013, 118(9):4716-4726.

453   Zhang Z, Zhao W, Tian J, et al. A mesoscale eddy pair southwest of Taiwan and its influence on

454   deep circulation[J]. Journal of Geophysical Research Oceans, 2013, 118(12):6479-6494.

455   Zhang Z, Zhao W, Tian J, et al. Spatial structure and temporal variability of the zonal flow in the

456   Luzon Strait[J]. Journal of Geophysical Research Oceans, 2015, 120(2).

457   Zhang Z, Zhao W, Qiu B, et al. Anticyclonic Eddy Sheddings from Kuroshio Loop and the

458   Accompanying Cyclonic Eddy in the Northeastern South China Sea[J]. Journal of Physical

459   Oceanography, 2017, 47(6):1243-1259.

460   Zhang H M, Reynolds R W, Bates J J, et al. Blended and gridded high resolution global sea

461   surface wind speed and climatology from multiple satellites: 1987-present. American

462   Meteorological Society 2006 Annual Meeting, Vol. 2. Https://www.ncei.noaa.gov/products

463   /blended-sea-winds

464

465

466

467